nature communications

Article

https://doi.org/10.1038/s41467-026-69279-2

Superior energy storage performance via engineering crossover region with competing orders in high-entropy multilayer capacitors

Received: 12 September 2025

Accepted: 27 January 2026

Published online: 11 February 2026

Check for updates

Tao Deng[1,2,3,10], Jiyang Xie[4,10], Zhen Liu[1,3] ✉, Liqiang He[5], Zhichao Hong[6], Haonan Peng[1,3], Dong Wang[5] ✉, Cosme Milesi-Brault[7], Teng Lu[8], Yonghong Chen[6], Zhisheng Lin[6], Wanbiao Hu[4], Brahim Dkhil[7], Yun Liu[8], Genshui Wang[1,2,3] ✉ & Junhao Chu[9]

As promising candidates for next-generation energy storage devices in electrical and electronic systems, lead-free multilayer ceramic capacitors face increasingly high performance requirements. To counteract the usual trade-off between energy storage density and efficiency, we here propose a high-entropy design that directly harnesses diverse oxide symmetries to targetedly engineer competing orders and tune the composition into the crossover region between relaxor ferroelectric and superparaelectric states. Atomic-scale structural analysis reveals high-entropy ceramic develops pronounced local polarization fluctuation and dispersed oxygen octahedral rotations, which enhance relaxor behavior and reduce switching barrier. Consequently, superior recoverable energy density of 20.64 J cm^{-3} and high efficiency of 94.2% are obtained in our designed high-entropy $Bi_{0.5}Na_{0.5}TiO_3$-based multilayer ceramic capacitors, along with excellent thermal/anti-fatigue stability and charge-discharge capabilities. This work provides a transferable strategy to engineer competing orders in lead-free dielectric materials and successfully achieves high-entropy multilayer ceramic capacitors with superior energy storage performance.

With the continuous booming of high-power electronics in recent years, lead-free energy-storage dielectric has garnered increasing research attention towards green power devices. Eco-friendly dielectric ceramics with fast discharge speed and performance stability, in comparison to supercapacitors, flywheels and batteries, exhibit huge advantages in energy storage applications[1–3]. Driven by the demands for high power density and extended cycling lifespan in advanced electronic systems, lead-free multilayer ceramic capacitors (MLCCs)

[1]Key Laboratory of Inorganic Functional Materials and Devices, Shanghai Institute of Ceramics, Chinese Academy of Sciences, Shanghai, China. [2]School of Chemistry and Materials Science, Hangzhou Institute for Advanced Study, University of Chinese Academy of Sciences, Hangzhou, China. [3]Science and Optoelectronics Engineering, University of Chinese Academy of Sciences, Beijing, China. [4]Yunnan Key Laboratory of Electromagnetic Materials and Devices, National Center for International Research on Photoelectric and Energy Materials, School of Materials and Energy, Yunnan University, Kunming, China. [5]Frontier Institute of Science and Technology and State Key Laboratory for Mechanical Behavior of Materials, Xi'an Jiaotong University, Xi'an, China. [6]Torch Electron Technology Co., LTD, Quanzhou, Fujian, China. [7]Laboratoire Structures, Propriétés et Modélisation des Solides (SPMS), Université Paris-Saclay, CentraleSupélec, CNRS, Gif-sur-Yvette, France. [8]Research School of Chemistry, The Australian National University, Canberra, ACT, Australia. [9]State Key Laboratory of Infrared Physics, Shanghai Institute of Technical Physics, Chinese Academy of Sciences, Shanghai, China. [10]These authors contributed equally: Tao Deng, Jiyang Xie. ✉e-mail: zhenliu@mail.sic.ac.cn; wang_dong1223@mail.xjtu.edu.cn; genshuiwang@mail.sic.ac.cn

have gained much research interest[4–6]. In general, the total energy density (W), the recoverable energy density (W_{rec}) and energy efficiency (η) of a dielectric can be calculated according to the equations: $W = \int_o^{P_{max}} EdP$, $W_{rec} = \int_P^{P_{max}} EdP$, $\eta = \frac{W_{rec}}{W} \times 100\%$, where E, P_{max} and P_r are the applied electric field, the maximum and remanent polarization, respectively[7,8]. Therefore, simultaneously achieving large P_{max}, low hysteresis loss and high breakdown electric field (E_b) is highly desired to realize high energy storage performance (ESP). In the past decade, various lead-free matrix materials have been explored to suit the needs of MLCCs, including $BaTiO_3$ (BT)[4], $NaNbO_3$ (NN)[5], $AgNbO_3$ (AN)[9], $BiFeO_3$ (BF)[10], $Bi_{0.5}Na_{0.5}TiO_3$ (BNT)[11]. Manufacturing textured ceramics and weakening polarization-strain coupling are regarded as useful approaches to enhance the performance of MLCCs[6,12]. For instance, textured ceramic was a proposed solution to enhance the breakdown strength of MLCCs by lowering the strains, but the low energy efficiency (η ~ 80%) did not own practical worth. Besides, W_{rec} of 14.6 J cm^{-3} and η of 93% were achieved in MLCCs with ultraweak polarization-strain coupling. One of the main issues for energy storage performance in MLCCs is finding the best balance between energy density (W_{rec} over 20 J cm^{-3}) and efficiency (η over 90%), as optimizing one parameter is typically achieved at the expense of sacrificing the other. This issue significantly hinders MLCCs development towards real applications for energy storage, restricting their potential for miniaturization and integration in next-generation device system.

The energy storage performance of MLCCs is highly dependent on dielectric types with distinct polarization behavior. The polarization response in classical ferroelectrics is closely associated with the long-range-order polarization configuration, which typically results in large hysteresis loss and unsatisfactory ESP[13–15]. Hence, relaxor ferroelectrics have been developed to realize high ESP via domain engineering. In relaxors, long-range ferroelectric order is broken and replaced by an amount of scattered polar nanoregions (PNRs), which suppress long-range dipole ordering under high electric field, resulting in field-insensitive dielectric constants and delayed polarization saturation[16–18]. Meanwhile, PNRs lower the domain-switching barrier and minimize hysteresis loss from a thermodynamic perspective[19,20]. Therefore, employing sophisticated strategies to transform ferroelectric domains into highly dynamic PNRs is widely regarded as key to simultaneously achieving high W_{rec} and η.

High-entropy strategy is recently emerging as a delicate approach for realizing relaxor ferroelectric that affords excellent compositional flexibility for improving energy storage performance owing to its unique effects[21–24]. Configurational entropy (S_{config}) is defined as $-R[\left(\sum_{i=1}^{N} y_i \ln y_i\right) + \left(\sum_{j=1}^{M} y_j \ln y_j\right)]$, where R, $N(M)$ and $y_{i(j)}$ are the ideal gas constant, atomic species and contents at the equivalent positions, respectively[25]. In most studies, high-entropy design is achieved by the incorporation of diverse cations into equivalent sites, facilitating the formation of a single perovskite structure within a stabilized lattice framework as S_{config} increases[26–28]. In general, mixing size- and charge-mismatched cations tends to generate heterogeneous nanoscale phases whose formation is difficult to control precisely, so that identifying useful compositions often relies on extensive trial-and-error. Moreover, this approach also tends to promote the excessive formation of weakly polar phases. As a result, superparaelectric or even paraelectric states appear at room temperature, accompanied by a dramatic decrease in dielectric constant (ε_r)[29,30]. However, low ε_r usually corresponds to small polarization saturation and thus relatively low ESP under practical operating fields. It is therefore highly desirable to develop novel high-entropy design strategies that can induce heterogeneous nanoscale phases while maintaining a high ε_r.

We proposed a high-entropy design strategy that engineers competing ferroic orders to achieve high energy storage performance in BNT-based MLCCs. Guided by phase-field simulation, we proportionally introduced various oxides with different symmetry, including $BaTiO_3$ (tetragonal phase, T)[31], $CaTiO_3$ (cubic phase, C), $SrTiO_3$ (C), $AgNbO_3$ (orthorhombic phase, O)[32] and $KNbO_3$ (O)[33], into a high spontaneous-polarization BNT (rhombohedral phase, R) matrix for tuning S_{config} (Fig. S1) of $(Bi_{0.5}Na_{0.5})_{(1-x)}(Sr_{0.2}Ca_{0.2}Ba_{0.2}K_{0.2}Ag_{0.2})_xTi_{1-0.4x}Nb_{0.4x}O_3$ (abbreviated as BNT-CE, named by their S_{config} value) system. Introducing symmetry-distinct oxide components into the same lattice targetedly gives rise to locally competing polar states. Consequently, it could lead to pronounced structural distortion and heterogeneity (Fig. 1a, b), thereby possibly enabling the formation of a crossover region between relaxor ferroelectric and superparaelectric states. This strategy is expected to concurrently enhance relaxor behavior and maintain large P_{max} in lead-free high-entropy MLCCs and therefore serves as an effective approach to simultaneously realize large W_{rec} and high η.

Results and discussion

Phase-field simulation of competing orders with high-entropy design

Herein, we employed phase-field simulation based on oxide-symmetry considerations to rationalize our compositional design and visualize the competing process of different polar orders[17,29,34]. To directly visualize the designed competing ferroic orders, we simulated the evolution of domains in both two- and three-dimensional space as a function of S_{config}. Distinct phase states and domain structures emerge upon the incorporation of various oxides with different phases into the matrix as displayed in Fig. 1c and Fig. S2. The distribution of simulated polarization vectors becomes gradually random with the increase of S_{config}, generating diverse polar regions. Based on the result of the competition among ferroic orders of $R/T/O/C$ phases represented by different vectors and colorful regions, the long-range order of the host phase is totally broken and transforms to nanoregions. Therefore, the high-entropy model manifests a heightened level of disorder. As the insets of Fig. 1d, e show, the evolution of the polar structure under an electric field reveals that the high-entropy model is much easier to revert to their initial state and maintains fast domain-switching speed with small hysteresis. In addition, corresponding simulated P-E loops are elucidated with increasing entropy (Fig. S3), revealing a remarkable transition from classic ferroelectric to relaxor ferroelectric and eventually to linear dielectric response. It also demonstrates that minimal P_r and high breakdown strength can be obtained as entropy increases (Fig. 1f). Besides, based on the simulated P-E loops, the W_{rec} and η are calculated in Fig. 1g as dependence on S_{config}. It shows the η gradually raises with increasing entropy while the highest W_{rec} is achieved at the S_{config} of 2.17R, beyond which W_{rec} begins to decline as the polarization response becomes weak and linear (Fig. S3). Meanwhile, the 2.17R model exhibits negligible variation in simulated P-E loops across a practical operating temperature range from −50 to 150 °C, demonstrating excellent thermal stability for application (Fig. S4). Therefore, these results highlight that optimizing S_{config} within an appropriate window is critical for forming competing orders and achieving superior energy storage performance.

Under the guidance of phase-field simulation, we prepared a series of $(Bi_{0.5}Na_{0.5})_{(1-x)}(Sr_{0.2}Ca_{0.2}Ba_{0.2}K_{0.2}Ag_{0.2})_xTi_{1-0.4x}Nb_{0.4x}O_3$ ceramics (BNT-CE, x = 0.02/0.85R, 0.1/1.27R, 0.2/1.65R, 0.3/1.94R, 0.4/2.17R, 0.5/2.34R). BNT-CE ceramics exhibit a pure perovskite structure with diffraction peaks regularly shifting towards low angle as S_{config} increases, indicative of lattice expansion (Fig. S5)[35,36]. However, for samples with entropy higher than 2.17R, Sr/Ca-rich secondary phase emerges, indicating that the solid solution limitation is reached[37]. Meanwhile, Rietveld refinements (Fig. S6) indicate that raising S_{config} reduces the R polar fraction, weakening the overall polarity of the BNT-CE ceramics. As revealed by Raman spectra (Fig. S7), the peak ν_2 representing the A-site vibration mode exhibits a red shift and reduced intensity with the increase of entropy, indicating enhanced random fields arising from A-site chemical complexity. The B-O (200-400 cm^{-1}) modes gradually broaden while BO_6-related modes (450-800 cm^{-1})

https://doi.org/10.1038/s41467-026-69279-2

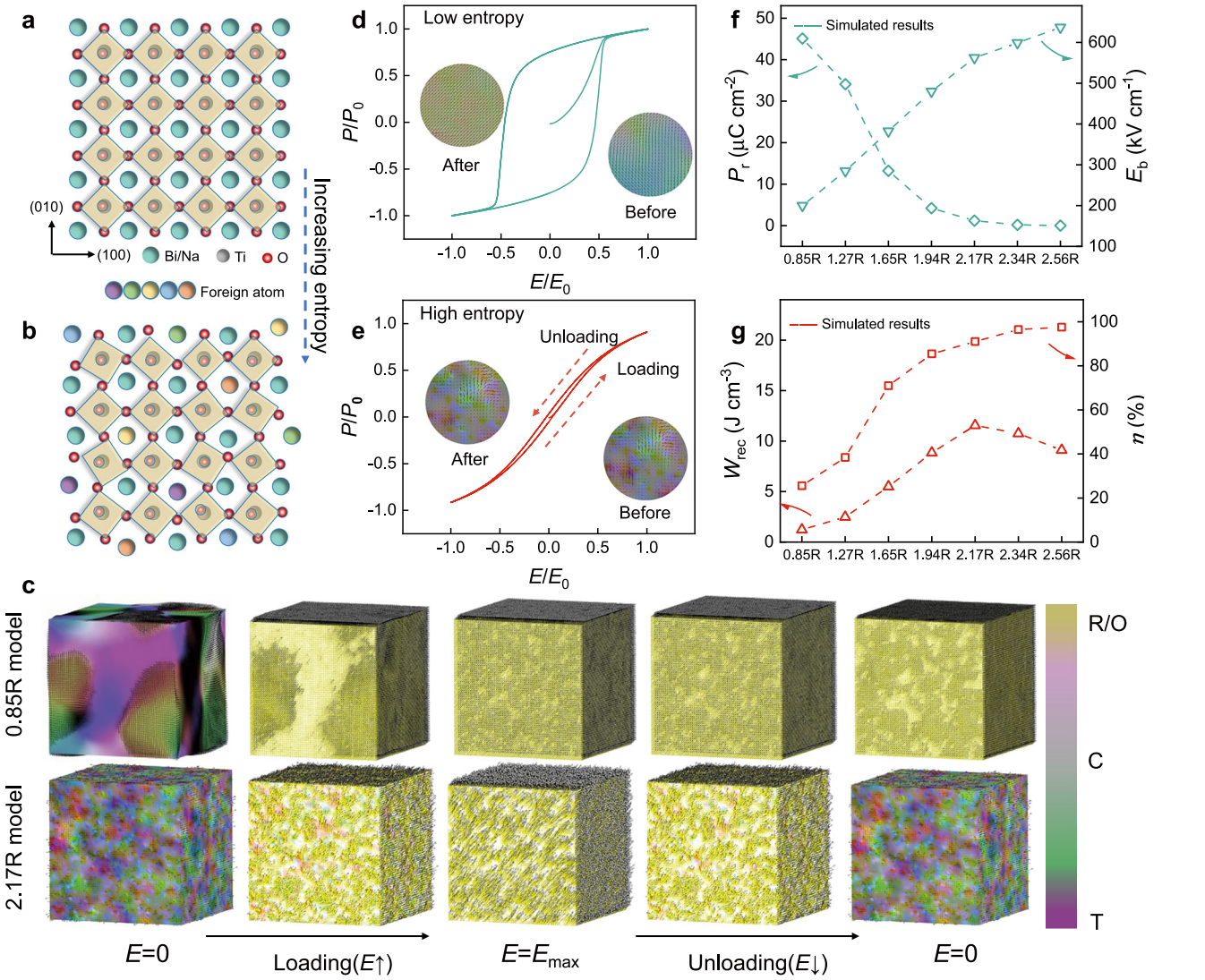

Fig. 1 | Phase-field simulation results for an entropy-driven perovskite structure along [001]. Schematic diagram of (**a**) Low-entropy model and (**b**) high-entropy model. **c** Three-dimensional domain structures of the 0.85R and 2.17R models under different electric fields by phase-field simulation. Simulated *P-E* loops of (**d**) the 0.85R and (**e**) 2.17R models. The insets illustrate domain states before and after electric field application. **f** Simulated evolution of P_r and E_b as functions of S_{config}. **g** Simulated evolution of W_{rec} and η as functions of S_{config}.

become narrower and more intense with the increase of S_{config}, which means short-range chemical disorder and dispersed octahedra distribution[38–40]. In order to evaluate the overall ESP, unipolar *P-E* loops of BNT-CE ceramics were measured at their characteristic E_b (Fig. 2a). Consistent with the simulation results, the transition from classical ferroelectric to relaxor ferroelectric is observed with increasing S_{config}, characterized by delayed polarization saturation. P_r is abruptly decreased from 44.7 to 1.1 μC cm^{-2} while P_{max} exhibits only a slight reduction from 60.9 to 60.5 μC cm^{-2}. Such negligible P_r and large P_{max} in high-entropy ceramic contribute to the improved ESP. Consequently, the 2.17R ceramic realizes high W_{rec} of 10.51 J cm^{-3} and high η of 88.2%, which are over 7- and 4- folds higher than those of the low-entropy 0.85R ceramic (Fig. 2b), respectively. In Fig. S8, the statistical E_b of BNT-CE ceramics were calculated by Weibull distribution fitting based on ten samples, with a good reliability supported by all the slopes β higher than 10[41]. The result shows that the E_b increases steadily from 243 kV cm^{-1} to 535 kV cm^{-1} with the increase of entropy. The average grain size of the BNT-CE ceramics decreases markedly from 1.42 μm to 0.63 μm with increasing S_{config} while the relative density of all samples increases only slightly from 96.8% to 97.4% (Fig. S9), owing to enhanced lattice strain energy and reduced driving force for grain coarsening[42]. Refined and dense microstructure helps to depress leakage current (Fig. S10), which induces enhanced barriers in carrier transport and diminishes the conduction loss at high electric field, thus substantially improving E_b[21]. To clarify the evolution of E_b in BNT-CE ceramics, we carried out finite-element simulations based on the SEM images (Fig. S9) to visualize the electric-field distribution and the propagation of electrical trees at 400 kV cm^{-1}, as shown in Fig. 2c[43]. The higher grain-boundary density in 2.17R ceramic provides more blocking and dissipation sites, which slows the propagation of electrical trees and therefore contributes to the decrease of leakage current and the higher breakdown strength.

The temperature-dependent dielectric properties of BNT-CE ceramics were then measured to evaluate their relaxor behavior (Fig. 2e and Fig. S11). A shoulder-like flat peak emerges as S_{config} reaches 1.65R and subsequently disappears for S_{config} higher than 1.65R, accompanied by a shift of the Curie temperature (T_m) towards lower temperature, which facilitates the coexistence of multiple phases and promotes domain switching[44,45]. Notably, by tuning S_{config}, the 2.17R ceramic is placed in the crossover region between relaxor ferroelectric

https://doi.org/10.1038/s41467-026-69279-2

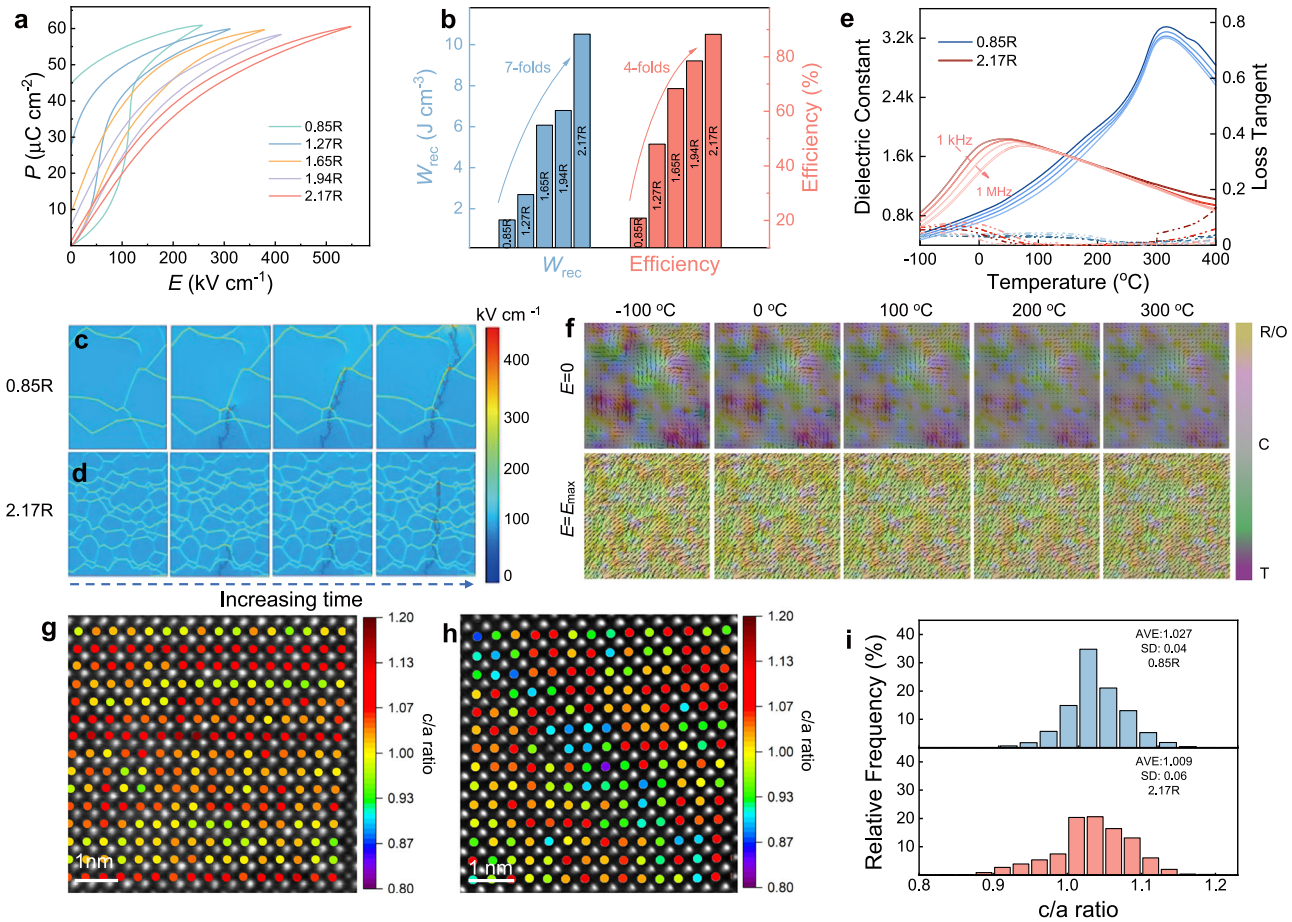

Fig. 2 | Energy storage performance and relaxor behavior of BNT-CE ceramic. **a** Unipolar *P-E* loops of BNT-CE ceramics with different S_{config}. **b** Comparison of W_{rec} and η with different S_{config}. Evolution of electric field and the growth of breakdown paths at the same electric field of 400 kV cm^{-1} for (**c**) the 0.85R and (**d**) 2.17R cerami. **e** Temperature-dependent dielectric constant and loss tangent of the 0.85R and 2.17R ceramics under different frequencies. **f** Simulated domain evolution of the 2.17R ceramic under various temperatures and electric fields. Mapping of unit cell c/a ratio of (**g**) the 0.85R and (**h**) 2.17R ceramics along the [001] direction. **i** Statistical c/a ratio distributions for the 0.85R and 2.17R ceramics.

and superparaelectric states with a high dielectric constant (~1800) at room temperature, rather than falling into a superparaelectric state with low ε_r as in many reported high-entropy systems[27,29,46]. In this crossover region, highly dynamic polar nanoregions and strong competition among ferroic orders allow a large polarization with a small remanent polarization and a high breakdown field[7,47]. Meanwhile, 2.17R ceramic exhibits excellent temperature coefficient of ε_r (within ± 15%) in −30 to 125 °C (Fig. S12), which meets the Y7R capacitor standard for application. Illustrated by the simulated domain evolution results of 2.17R model during a wide temperature span of −100 to 300 °C (Fig. 2f), the fraction of *C* phase (gray region) gradually increases with rising temperature, while the polarization configuration under maximum electric field keeps unvaried across all temperatures. To further elucidate the variation of relaxor behavior, the diffuseness coefficient γ is fitted by the modified Curie-Weiss equation: $\frac{1}{\varepsilon}-\frac{1}{\varepsilon_m}=\frac{(T-T_m)^{\gamma}}{C}$[48]. The magnitude of γ increases from 1.03 to 1.91 as S_{config} increases (Fig. S13), supporting the enhanced relaxor behavior in 2.17R high-entropy ceramic[17]. The dynamic domain responses of the 0.85R and 2.17R ceramics were also measured by piezo-response force microscopy (PFM) to monitor the evolution of ferroelectric domains (Fig. S14). With increasing entropy, the switched domains induced by a 20 V electric field fade more rapidly and are more readily reverted to their initial configuration upon field removal, indicating shorter relaxation time and low hysteresis loss in 2.17R high-entropy ceramic[46,49]. In addition, we calculated the distribution of the unit cell c/a ratio to clarify the structural origin of this crossover and the enhanced breakdown strength through HAADF-STEM analysis (Fig. 2g, h). The average c/a ratio significantly decreases from 1.027 for the 0.85R ceramic to 1.009 for the 2.17R ceramic, as shown in Fig. 2i, which indicates weak long-range ferroelectric anisotropy and polarization-strain coupling in the 2.17R ceramic[50]. The reduced average c/a helps to diminish local field amplification and thermal loss under high electric field, which is beneficial for improving breakdown strength[39]. Moreover, the 2.17R ceramic exhibits a dispersed distribution of c/a ratio, in contrast to the more clustered distribution observed in the 0.85R ceramic, with the standard deviation increasing from 0.04 (0.85R) to 0.06 (2.17R) as entropy rises, which indicates stronger spatial heterogeneity of lattice distortion.

Local structural evolution of entropy-driven ceramics

As revealed in phase-field simulations, competing orders generated by chaotic chemical environments and distorted local structure serve as the structural foundation for achieving high energy storage performance. Thus, the evolutions of polarization configuration in both high-entropy and low-entropy ceramics were systematically investigated to elucidate the underlying polarization response mechanism through high-angle annular dark-field scanning transmission electron microscopy (HAADF-STEM). The atomic-resolution images of the 0.85R

https://doi.org/10.1038/s41467-026-69279-2

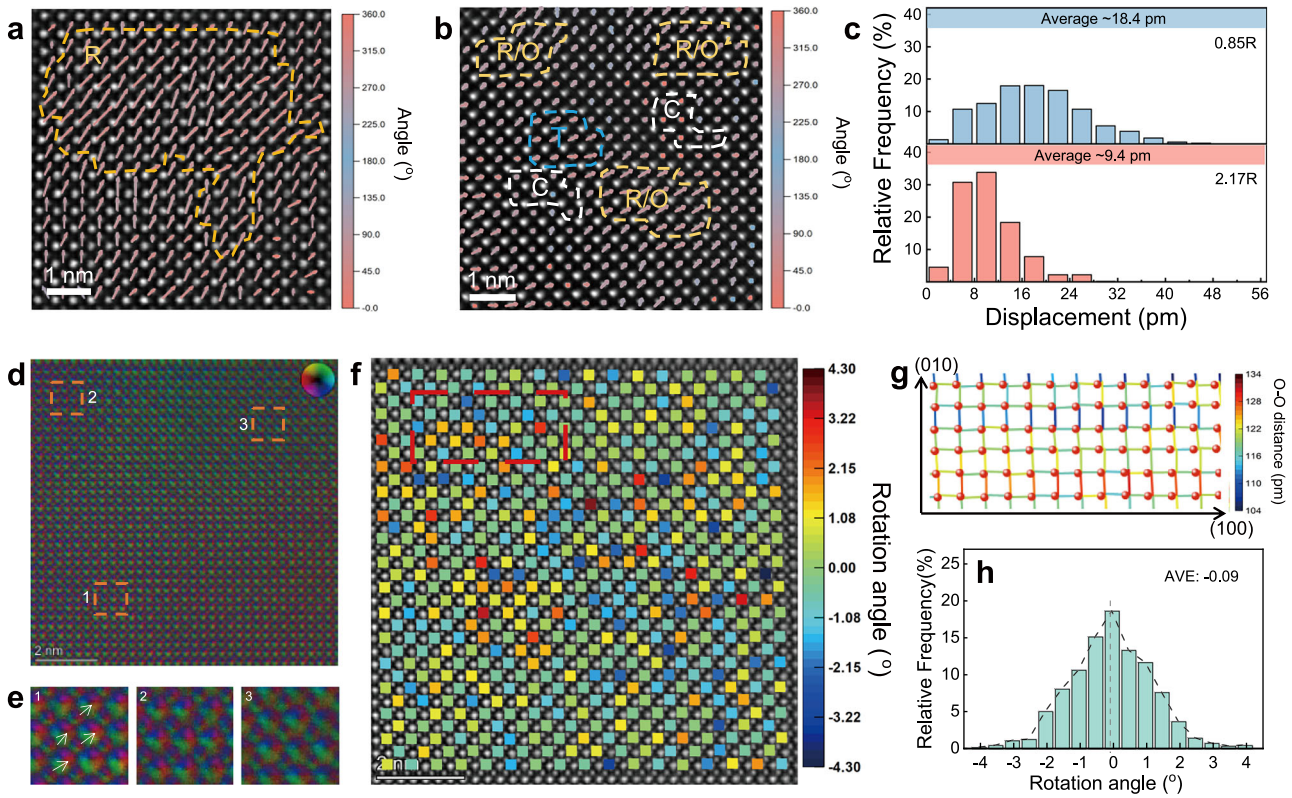

Fig. 3 | Local structural evolution in BNT-CE ceramics and the BO_6 octahedral distortion in high-entropy ceramic. Atomic-resolution HAADF-STEM polarization vector image along [001] direction of (**a**) the 0.85R and (**b**) 2.17R ceramics. **c** Polarization displacement of the 0.85R and 2.17R ceramics. **d** DPC image with diverse characteristics of *E*-field distribution and (**e**) enlarged images of the regions in (**d**). **f** iDPC image of A/B sites and oxygen ions along [001] direction of the 2.17R high-entropy ceramic, and the colorful squares represent the BO_6 with different rotation angle. **g** Distance and relative position of adjacent O atoms of the enclosed region in (**f**). **h** Statistical result of the rotation angle distribution of the BO_6 octahedral of the 2.17R ceramic.

(Fig. 3a) and 2.17R (Fig. 3b) ceramics along [001] are marked by colorful vectors, which represent the polarization angle of the B-site cations relative to the lattice centers of the four nearest neighboring A-site cations[8]. The 0.85R ceramic exhibits pronounced polarization displacement (Fig. 3c) and large domain sizes, with the *R* phase as the dominant phase. With increasing S_{config}, the notable reduction of *R*/*O* phase, combined with the existing tiny amount of *T* phase and increased fraction of *C* phase induce the competition of diverse ferroic orders within local regions. Compared to the low-entropy ceramic, the remarkable distinction in polarization orientation of high-entropy ceramic reflects substantial structural distortion and diverse heterogeneous polarization configuration, wherein strongly polar phases are intricately embedded within a weakly polar cubic matrix. Figure 3c stresses a contrast in the displacement distribution that the average displacement of ~ 9.4 pm in the 2.17R ceramic is much smaller than that of ~ 18.4 pm in the 0.85R ceramic. This trend is consistent with the grain-size evolution (Fig. S9), where smaller grains are expected to confine the polarization correlation length and suppresses domain coalescence[51]. This reduced polarization displacement promotes complex interactions among randomly distributed ions and competing ferroic orders, giving rise to highly dynamic polar nanoregions with weak domain coupling[22,49,52]. Therefore, tuning configurational entropy to induce local compositional inhomogeneity provides an effective way to regulate the formation of competing orders and to modulate the associated structural distortions. To comprehensively clarify structural features in local polar fluctuations of BNT-CE ceramic, we discerned the local *E*-field distribution by differential phase contrast (DPC) analysis[12]. The DPC-STEM (Fig. 3d) image of the 2.17R ceramic shows rapidly varying hues in the local electric-field distribution, with color indicating the field direction and brightness representing its magnitude. The pronounced fluctuations in both color and brightness highlight the polar heterogeneity of the local fields. Three representative types of *E*-field distribution are observed, as displayed in Fig. 3e, which can be associated with polar regions (region 1), disordered polar nanoregions (region 2) and weakly polar matrix (region 3), respectively. These distinct *E*-field distributions reflect the presence of different local polar states within the crossover region. It directly visualizes the coexisting polar states that arise from competing ferroic orders in the high-entropy ceramic, which is favorable for achieving high saturation polarization and low polarization hysteresis.

We also utilized integrated differential phase contrast (iDPC) to particularly capture the otherwise imperceptible light O atoms, in order to directly analyze the rotation behavior of BO_6[53]. The O atoms can be discernible in the iDPC images because this technique offers high sensitivity to light elements, and the relatively small contrast difference with neighboring cations enhances their visibility[54]. Figure S15 gives the high-resolution iDPC image of 2.17R high-entropy ceramic along [001] direction and illustrates the atom occupancy of the A/B site and O position. The squares with various colors in Fig. 3f denote different BO_6 rotation behaviors, revealing irregular alternations between clockwise and anticlockwise orientation. As seen in Fig. 3g, O atoms within the same horizontal layer display varying displacement amplitudes, accompanying by noticeable differences in adjacent O-O distance. Then, the O-O distances (Fig. S16) extracted from the iDPC image are statistically analyzed, which demonstrates that most O atoms deviate from their average positions. This reflects a random and diffuse distribution of oxygen displacements. Quantitatively, octahedral rotation angles range from −4.3 to +4.3°, indicating

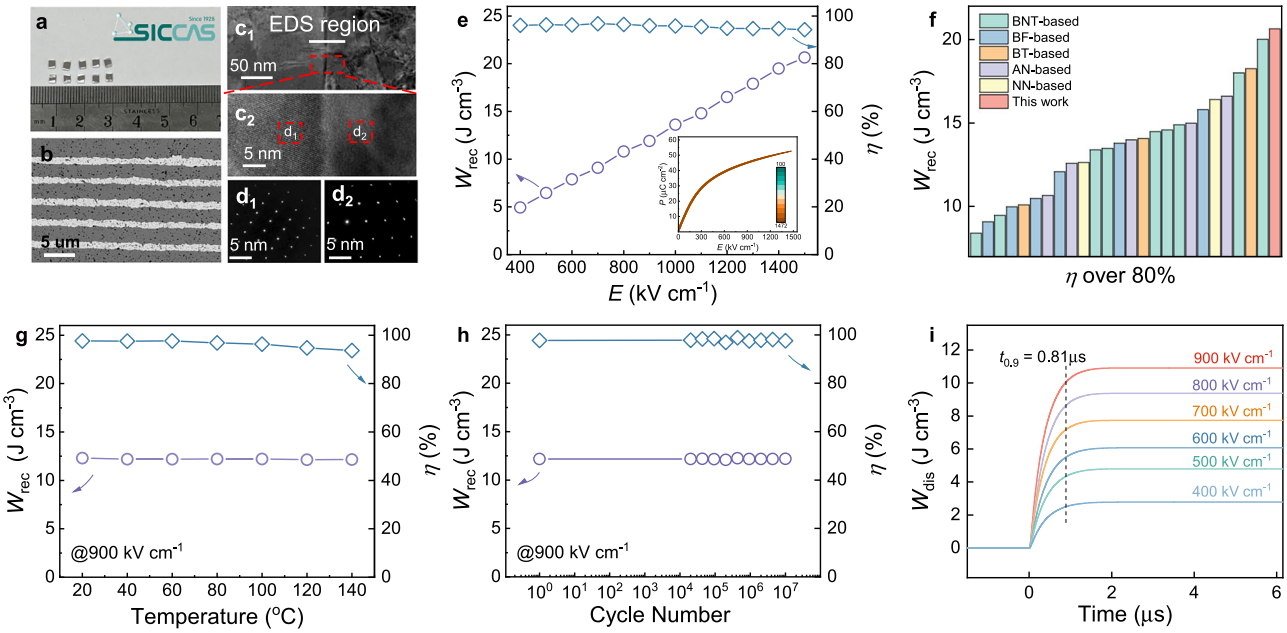

Fig. 4 | Microstructures and energy storage performance of high-entropy 1210-type MLCCs. a Optical photo of high-entropy MLCCs. **b** SEM image of high-entropy MLCCs. TEM images for ($\mathbf{c}_1$) low resolution and ($\mathbf{c}_2$) high resolution, ($\mathbf{d}_1$-$\mathbf{d}_2$) SAED pattern acquired from the electrode area marked in ($\mathbf{c}_2$). **e** W_{rec} and η of the MLCCs under different electric fields. The inset is the corresponding *P-E* loops. **f** Comparison of energy storage performance in this work with other recently reported MLCCs. **g** Thermal stability of W_{rec} and η as temperature increases. **h** Anti-fatigue stability of W_{rec} and η as cycling number increases. **i** Time-dependent discharge energy density under various electric fields for high-entropy MLCCs.

relatively small rotation with a non-collective distribution. The statistical histogram in Fig. 3h presents a normal distribution of the octahedra, further confirming the dispersed and random nature of octahedral rotations in high-entropy ceramic. This heterogeneity of octahedral rotation caused by competing orders locally disrupts long-range symmetry and shifts the positive/negative charge center, generating spatially dispersed local dipoles and reduced switching barriers[55]. Such a configuration delays polarization saturation and facilitates reversible domain switching, thereby sustaining a large P_{max}. Furthermore, local distortions of the oxygen octahedra will consume a portion of the electrical energy required for establishing relatively large domains under an applied field[23], thus impeding domain growth and delaying saturation polarization. The structural variations by increasing S_{config} promote the formation of a weakly polar region, thereby lowering the energy barrier for reorienting the polarization configuration. Thus, the designed competing orders induced by high-entropy strategy modulate oxygen octahedral rotations, which delays polarization saturation and enhances breakdown strength, thereby maintaining a large P_{max} while reducing P_r and enhancing ESP.

Energy Storage Performance of high-entropy MLCCs

To validate the efficacy of the entropy-induced strategy for actual pulse power application, we further fabricated 1210-type MLCCs comprising four active ceramic layers, based on the optimal composition of S_{config} = 2.17R. Figure 4a, b and Fig. S17 present the SEM image and energy-dispersive X-ray spectroscopy (EDS) element mapping of the high-entropy multilayer capacitor, which shows a uniform thickness of ~ 5.5 μm in the dielectric layer and 1.5 μm in the electrode layer, respectively. Both dielectric layers and electrode layers exhibit a dense microstructure, and the elements in each layer are uniformly distributed. The selected area electron diffraction (SAED) was conducted in the interface region between the two layers (Fig. 4(c_1-c_2)), which exhibits a well-defined and sharp boundary. No obvious element diffusion can be found between the dielectric layer and the electrode layer according to the result of linear scanning (Fig. S18), and both regions exhibit sharp diffraction spots (Fig. 4(d_1-d_2)). The inset of Fig. 4e and Fig. S19 show the unipolar *P-E* loops of high-entropy MLCCs as a function of *E* field. High W_{rec} ~ 20.64 J cm^{-3} and η ~ 94.2% are achieved in high-entropy MLCCs at a high E_b of 1472 kV cm^{-1}. As Fig. 4f reveals, our work represents superior energy storage performance compared to other MLCCs in recent reports. To quantitatively evaluate the trade-off between W_{rec} and η, we used a figure of merit $U_F = W_{rec}/(1-\eta)$ to reflect the overall energy storage performance[2], as shown in Fig. S20. U_F of our work reaches a high value of 355.7 owing to the combined high W_{rec} and η. Hence, these results demonstrate the effectiveness of regulating competing orders via a high-entropy strategy in realizing superior energy-storage-performance MLCCs.

From a practical application viewpoint, we also evaluated the thermal stability and cycle reliability of the high-entropy MLCCs. In Fig. 4g and Fig. S21, we tested the temperature stability of energy storage performance at the electric field of 900 kV cm^{-1} in the range from 20 to 140 °C, which shows a high W_{rec} of ~ 12.21 J cm^{-3} and η of over 93.3%, respectively, and displays a slight degradation below 5% for both W_{rec} and η. Besides, the anti-fatigue reliability tests were conducted to further assess the practical application. As shown in Fig. 4h, the MLCCs survive after 10^7 cycles with only below 2% attenuation, keeping a W_{rec} of ~ 12.15 J cm^{-3} and η of over 96.2%. In addition, as a key parameter, the charge-discharge performance of high-entropy MLCCs was measured at different electric field. Figure 4i and Fig. S22 illustrate the overdamped discharge curves of the high-entropy MLCCs within the field range of 200 kV cm^{-1} to 900 kV cm^{-1}, where MLCCs achieve a large discharge energy density (W_{dis}) of 10.92 J cm^{-3} with a fast $t_{0.9}$ ~ 0.81 μs (the time to release 90% of W_{dis}). Meanwhile, high-entropy MLCCs exhibit high current density (C_D) of 424 A cm^{-2} and large power density (P_D) of 191 MW cm^{-3} (Fig. S23). The charge-discharge performance exceeds that of most reported MLCCs, as shown in Fig. S24. The excellent temperature, fatigue stability and charge-discharge property fully show wide application scenarios and huge application potential for the next-generation MLCC devices.

In summary, we demonstrated a high-entropy design that directly harnessed the symmetry of different oxides, together with phase-field simulations, to engineer competing polar orders and form the crossover region. At the local scale, the competition among diverse orders yields more dispersed and random polar configuration with the increase of S_{config}. In composition with optimized S_{config} value, distinct *E*-field distributions, oxygen displacements and dispersed distribution of BO_6 rotations are observed, and these features together contribute to broad switching barrier and enhanced relaxor behavior. Ultimately, superior performance of W_{rec} ~ 20.64 J cm^{-3} and η ~ 94.2% is achieved in high-entropy MLCCs, along with excellent temperature and fatigue stability, and a large charge-discharge capacity of W_{dis} ~ 10.92 J cm^{-3}. Our work provides a predictive and transferable solution to the long-standing challenge of simultaneous improvement of W_{rec} and η in pulse capacitors and highlights a broader technological potential for high-entropy multilayer devices in next-generation energy-storage applications.

Methods

Phase-field simulation and finite-element simulation

The total free energy of the high-entropy BNT-based system can be expressed as the sum of the following contributions[56,57]: $F = \int f_{landau}dV + f_{grad}dV + f_{elas}dV + f_{elec}dV$. The Landau free energy f_{lan} can be presented as function of $\mathbf{P_i}$ as: $f_{landau} = \alpha_1\left(P_1^2+P_2^2+P_3^2\right) + \alpha_{11}\left(P_1^4+P_2^4+P_3^4\right) + \alpha_{12}\left(P_1^2P_2^2+P_2^2P_3^2+P_1^2P_3^2\right) + \alpha_{111}\left(P_1^6+P_2^6+P_3^6\right) + \alpha_{112}\left(P_1^4P_2^2+P_2^4P_3^2+P_1^4P_3^2+P_1^2P_2^4+P_2^2P_3^4+P_1^2P_3^4\right) + \alpha_{113}(P_1^2P_2^2P_3^2)$, where α is the Landau coefficients. f_{grad} is the gradient energy, representing the domain boundary energy, which can be defined as: $f_{grad} = \frac{1}{2}G\sum_{i,j}^{3}(\mathbf{P_{ij}})^2$, where G is the gradient energy coefficient. The long-range elastic interactions energy f_{elas}, including strain-gradient and external-stress fields, is expressed as: $f_{elas} = \frac{1}{2}\left\{C_{ijkl}\left(\varepsilon_{ij}-\varepsilon_{ij}^0\right)\left(\varepsilon_{kl}-\varepsilon_{kl}^0\right) + C_{ijkl}e'_{ij}\left(\varepsilon_{kl}-\varepsilon_{kl}^0\right)\right\}$, where C_{ijkl} is the elastic stiffness tensor, ε_{ij}, ε^0_{ij} and e'_{ij} are the total strain. $f_{elec} = -\frac{1}{2}E_iP_i - \frac{1}{2}E_{i,depol}\overline{P_i}$, where E_i represents the inhomogeneous electric field caused by dipole-dipole interactions, $E_{i,depol}$ is the average depolarization field. $\overline{P_i}$ is the average polarization. The temporal evolution of the polarization field can be calculated by solving the time-dependent Ginzburg-Landau (TDGL) equation: $\frac{dP_i(x,t)}{dt} = -M\frac{\delta F}{\delta P_i(X,t)}, i = 1,2,3$, where M is the kinetic coefficient related to the domain mobility, t is time, and i denotes polarization variants. Phase-field simulations were performed in a three-dimensional grid of size $64 \times 64 \times 64$ and in the length scale l_0 (the numerical grid size) of ~ 2.0 nm with periodic boundary conditions. The probability of the electrical tree channels is defined using the following equation: $p(i',j' \rightarrow i,j) = \frac{(\aleph_{i',j'}-\aleph_{i,j}-\aleph)^m}{\sum(\aleph_{i',j'}-\aleph_{i,j}-\aleph)^m} + (\aleph_{i',j'} - \aleph_{i'',j''} - \aleph)^m - loss$, where $\aleph_{i,j}$, $\aleph_{i',j'}$ and $\aleph_{i'',j''}$ represent the electrical potential of the discharged point, probable point, and linked point, respectively. $\aleph$ is the threshold electrical potential of the ceramic for the grain and grain boundary. Loss and m denote the evolution loss of the tip electrical tree channels and the fractal dimension, respectively.

Ceramic preparation

A conventional solid sintering was used to prepare $(Bi_{0.5}Na_{0.5})_{(1-x)}(Sr_{0.2}Ca_{0.2}Ba_{0.2}K_{0.2}Ag_{0.2})_xTi_{1-0.4x}Nb_{0.4x}O_3$ ceramics (x = 0.02, 0.1, 0.2, 0.3, 0.4, 0.5). The raw powders of Bi_2O_3 (99.99%), Na_2CO_3 (99.8%), $BaCO_3$ (99.95%), $SrCO_3$ (99.99%), $CaCO_3$ (99.99%), Ag_2O (99.7%), K_2CO_3 (99%), TiO_2 (99.9%), Nb_2O_5 (99.99%) were mixed and milled for 4 hours by using ZrO_2 balls in ethanol. Subsequently, the dried powder was then calcined in an alumina crucible at 850 °C for 2 h. Powders were milled again using smaller size ZrO_2 balls, and 0.3 wt.% $MnCO_3$ was added as the sintering aid. Then, the calcined powders were mixed with 6 wt.% polyvinyl alcohol. The green pellet was first burn out binder at 600 °C for 2 h and finally sintered at 1120-1180 °C for 2 h in an oxygen atmosphere.

MLCC preparation

BNT-based high-entropy powder (x = 0.4/2.17R) was utilized in the fabrication of 1210-type MLCCs via tape casting with an MTI MSK-AFA-II system. A 70 Ag/30 Pd electrode was printed via a DEK 247 screen printer. The stacked layers were then subjected to hot-pressing at 80 °C for 20 min. The resulted MLCCs were sintered at 1080 °C for 2 h in an oxygen atmosphere.

Structure characterizations

Powder X-ray diffraction patterns were collected using a powder X-ray diffractometer (XRD, Rigaku, D/max-2550 V) with Cu Kα radiation (λ = 1.5406 Å). Raman spectra were obtained with a Raman spectrometer (Renishaw, inVia). Field-emission scanning electron microscopy (FE-SEM, Hitachi, S-4800, Tokyo, Japan) was used to examine the microstructures and density of the ceramics. Apparent density of all ceramic samples was measured by the vacuum-saturated Archimedes method. The theoretical density was determined from the unit-cell parameters obtained by Rietveld refinement of the diffraction peaks. The relative density is the ratio of the apparent density and the theoretical density. The STEM and DPC/iDPC tests were carried out on a 300 kV Thermofisher Spectra 300 electron microscope equipped with double aberration correctors. During the process of testing, the probe convergence angle was 18 mrad, and the collection angle was 50-200 mrad to obtain the HAADF images. For determining the B-site cation displacement vectors and rotation of BO_6 octahedra, the noise in the obtained HAADF-STEM and DPC/iDPC images was reduced by Gaussian blur of Velox (Thermofisher) software with sigma of 1.0-1.8. The projected atom positions of A sites, B sites, and O were determined via OpenCV using the Python software, thus, the projected B-site cation displacement was deduced as a vector between each B-site cation and the center of mass of its four nearest corner A-site cations. The rotation of BO_6 octahedra was deduced as an angle from the minimum inscribed square of each B-site cation and its four nearest O ions with [001] direction.

Ferroelectric and dielectric measurements

P-E loops were measured using ceramic samples with an electrode size of 1 mm diameter and a thickness of ~ 60 μm under an alternating current voltage with a frequency of 10 Hz by using a ferroelectric measuring system (aixACCT TF Analyzer 2000E). A broad frequency dielectric spectrometer (Novocontrol GmbH, Concept 80) was used to measure temperature- and frequency-dependent dielectric properties. Underdamped and overdamped charge-discharge tests were conducted on a commercial charge-discharge platform (CFD-001, Gogo Instruments Technology, Shanghai, China) using an RLC load circuit under a direct current voltage, operated at a 1 kHz. We calculated charge-discharge properties by employing the following formula: $W_{dis} = \frac{R\int I^2(t)dt}{V'}$, $C_D = \frac{I_{max}}{S}$ and $P_D = \frac{E\times I_{max}}{2S}$, where S represents the effective electrode area and V' is the effective volume of the tested samples.

Data availability

All data supporting this study and its findings are available within the article and its Supplementary Information. The data that support the findings of this study are available on request from the corresponding authors.

References

1. Shu, L. et al. Partitioning polar-slush strategy in relaxors leads to large energy-storage capability. *Science* **385**, 204 (2024).
2. Zhang, M. et al. Ultrahigh energy storage in high-entropy ceramic capacitors with polymorphic relaxor phase. *Science* **384**, 185 (2024).
3. Luo, N. et al. Ordering-Structured Antiferroelectric Composite Ceramics for Energy Storage Applications. *Adv. Mater.* **37**, 2420258 (2025).
4. Zhao, P. et al. Ultra-high energy storage performance in lead-free multilayer ceramic capacitors via a multiscale optimization strategy. *Energy Environ. Sci.* **13**, 4882–4890 (2020).
5. Lv, Z. et al. $NaNbO_3$-Based multilayer ceramic capacitors with ultrahigh energy storage performance. *Adv. Energy Mater.* **14**, 2304291 (2024).
6. Li, J. et al. Grain-orientation-engineered multilayer ceramic capacitors for energy storage applications. *Nat. Mater.* **19**, 999–1005 (2020).
7. Jayakrishnan, A. R. et al. Are lead-free relaxor ferroelectric materials the most promising candidates for energy storage capacitors?. *Prog. Mater. Sci.* **132**, 101046 (2023).
8. Yang, B. et al. Engineering relaxors by entropy for high energy storage performance. *Nat. Energy* **8**, 956–964 (2023).
9. Zhu, L. F. et al. Heterovalent-doping-enabled atom-displacement fluctuation leads to ultrahigh energy-storage density in $AgNbO_3$-based multilayer capacitors. *Nat. Commun.* **14**, 1166 (2023).
10. Lu, Z. et al. Superior energy density through tailored dopant strategies in multilayer ceramic capacitors. *Energy Environ. Sci.* **13**, 2938–2948 (2020).
11. Ji, H. et al. Ultrahigh energy density in short-range tilted NBT-based lead-free multilayer ceramic capacitors by nanodomain percolation. *Energy Storage Mater.* **38**, 113–120 (2021).
12. Zhang, L. et al. Ultra-Weak Polarization-Strain Coupling Effect Boosts Capacitive Energy Storage. *Adv. Mater.* **36**, 2406219 (2024).
13. Wei, K. et al. Enhancing comprehensive energy storage properties in Pb-free relaxor AFE/FE system via heterogeneous structure tuning and defect engineering. *Acta Mater.* **278**, 120278 (2024).
14. Deng, T. et al. Excellent energy-storage performance in $Bi_{0.5}Na_{0.5}TiO_3$-based lead-free composite ceramics via introducing pyrochlore phase $Sm_2Ti_2O_7$. *Chem. Eng. J.* **465**, 142992 (2023).
15. Xu, J. et al. Superior energy storage performance in a self-organized trirelaxor-antiferroelectric nanocomposite over a wide temperature range. *Adv. Mater.* **37**, 2502788 (2025).
16. Krogstad, M. J. et al. The relation of local order to material properties in relaxor ferroelectrics. *Nat. Mater.* **17**, 718–724 (2018).
17. Zhao, W. et al. Broad-high operating temperature range and enhanced energy storage performances in lead-free ferroelectrics. *Nat. Commun.* **14**, 5725 (2023).
18. Liu, Y. et al. Ultrahigh capacitive energy storage through dendritic nanopolar design. *Science* **388**, 211 (2025).
19. Liu, M. et al. Superior energy-storage performance in $BaTiO_3$-$AgNbO_3$ binary relaxor via the competitions of multiple polar orders. *Acta Mater.* **289**, 120943 (2025).
20. Li, Y. et al. Domain dynamics response to polarization switching in relaxor ferroelectrics. *Adv. Mater.* **36**, 2411467 (2024).
21. Schweidler, S. et al. High-entropy materials for energy and electronic applications. *Nat. Rev. Mater.* **9**, 266–281 (2024).
22. Hsu, W. L., Tsai, C. W., Yeh, A. C. & Yeh, J. W. Clarifying the four core effects of high-entropy materials. *Nat. Rev. Chem.* **8**, 471–485 (2024).
23. Chen, L. et al. Giant energy-storage density with ultrahigh efficiency in lead-free relaxors via high-entropy design. *Nat. Commun.* **13**, 3089 (2022).
24. Wei, K. et al. Collaborative design of polarization and antiferrodistortion configurations in high energy capacitive relaxor ferroelectrics. *Nat. Commun.* **16**, 7833 (2025).
25. Zhao, B. et al. High-entropy enhanced microwave attenuation in titanate perovskites. *Adv. Mater.* **35**, 2210243 (2023).
26. Li, W. et al. Generative learning facilitated discovery of high-entropy ceramic dielectrics for capacitive energy storage. *Nat. Commun.* **15**, 4940 (2024).
27. Wei, T. et al. High-entropy assisted capacitive energy storage in relaxor ferroelectrics by chemical short-range order. *Nat. Commun.* **16**, 807 (2025).
28. Zeng, X. et al. Giant Capacitive Energy Storage in High-Entropy Lead-Free Ceramics with Temperature Self-Check. *Adv. Mater.* **36**, 2409059 (2024).
29. Peng, H. et al. High-entropy relaxor ferroelectric ceramics for ultrahigh energy storage. *Nat. Commun.* **15**, 5232 (2024).
30. Wang, C., Cao, W., Liang, C., Zhao, H. & Wang, C. Equimolar high-entropy for excellent energy storage performance in $Bi_{0.5}Na_{0.5}TiO_3$-based ceramics. *Energy Storage Mater.* **70**, 103534 (2024).
31. Smith, M. B. et al. Crystal structure and the paraelectric-to-ferroelectric phase transition of nanoscale $BaTiO_3$. *JACS* **130**, 6955–6963 (2008).
32. Hu, Z. et al. Designing silver niobate-based relaxor antiferroelectrics for ultrahigh energy storage performance. *J. Adv. Ceram* **13**, 1282–1290 (2024).
33. Matsudo, H., Kakimoto, K. -i & Kagomiya, I. Thermal depolarization measurement for $Na_{0.5}K_{0.5}NbO_3$ piezoceramics. *Jpn. J. Appl. Phys.* **49**, 09MC07 (2010).
34. Li, D. et al. A high-temperature performing and near-zero energy loss lead-free ceramic capacitor. *Energy Environ. Sci.* **16**, 4511–4521 (2023).
35. Bilal, M. K. et al. A novel relaxor $(Bi,Na,Ba)(Ti,Zr)O_3$ lead-free ceramic with high energy storage performance. *J. Am. Ceram. Soc.* **104**, 3982–3991 (2021).
36. Zhao, H. et al. High-entropy design toward ultrahigh energy storage density under moderate electric field in bulk lead-free ceramics. *Adv. Funct. Mater.* **35**, 2411954 (2024).
37. Kornphom, C., Saenkam, K. & Bongkarn, T. Enhanced energy storage properties of BNT-ST-AN relaxor ferroelectric ceramics fabrication by the solid-state combustion technique. *Phys. Stat. Sol.* **220**, 2200240 (2022).
38. Jain Ruth, D. E. & Sundarakannan, B. Structural and Raman spectroscopic studies of poled lead-free piezoelectric sodium bismuth titanate ceramics. *Ceram. Int.* **42**, 4775–4778 (2016).
39. Zhang, H. et al. Origin of polarization in bismuth sodium titanate-based ceramics. *JACS* **146**, 5569–5579 (2024).
40. Li, J. et al. Enhanced energy-storage in lead-free multilayer capacitors via entropy-assisted polymorphic domain engineering. *Nat. Commun.* **16**, 8580 (2025).
41. Peng, H. et al. Superior energy density achieved in unfilled tungsten bronze ferroelectrics via multiscale regulation strategy. *Adv. Sci.* **10**, 2300227 (2023).
42. Oses, C., Toher, C. & Curtarolo, S. High-entropy ceramics. *Nat. Rev. Mater.* **5**, 295–309 (2020).
43. Gao, S. et al. Ultrahigh energy density and excellent discharge properties in Ce^{4+} and Ta^{5+} co-modified $AgNbO_3$ relaxor antiferroelectric ceramics via multiple design strategies. *Acta Mater.* **246**, 118730 (2023).
44. Bai, W. et al. Temperature-insensitive large strain response with a low hysteresis behavior in BNT-based ceramics. *Ceram. Int.* **42**, 7669–7680 (2016).
45. Liu, G. et al. Phase evolution in $(1-x)(Na_{0.5}Bi_{0.5})TiO_3$-$xSrTiO_3$ solid solutions: A study focusing on dielectric and ferroelectric characteristics. *J. Materiomics* **6**, 677–691 (2020).
46. Liu, J. et al. Ferroelectric tungsten bronze-based ceramics with high-energy storage performance via weakly coupled relaxor design and grain boundary optimization. *Nat. Commun.* **15**, 8651 (2024).

47. Yuan, R. et al. Optimizing electrocaloric effect in barium titanate-based room temperature ferroelectrics: combining Landau theory, machine learning and synthesis. *Acta Mater.* **235**, 118054 (2022).
48. Liu, M. et al. Weakly coupled relaxor construction in lead-free ferroelectrics with simple composition for superior energy-storage performance. *Mater. Horiz.* **12**, 3939 (2025).
49. Deng, T. et al. Ultrahigh energy storage performance in BNT-based binary ceramic via relaxor design and grain engineering. *Energy Storage Mater.* **71**, 103659 (2024).
50. Liu, Y. et al. Radiation-hardened dendritic-like nanocomposite films with ultrahigh capacitive energy density. *Nat. Commun.* **16**, 3882 (2025).
51. Qian, J. et al. Interfacial coupling boosts giant electrocaloric effects in relaxor polymer nanocomposites: in situ characterization and phase-field simulation. *Adv. Mater.* **31**, e1801949 (2019).
52. Cao, W. et al. A strategy of enhancing polarization to achieve excellent energy storage performance in simple $Bi_{0.5}K_{0.5}TiO_3$-based relaxors. *Angew. Chem. Int. Ed. Engl.* **64**, 202500516 (2025).
53. Kumar, A. et al. Atomic-resolution electron microscopy of nanoscale local structure in lead-based relaxor ferroelectrics. *Nat. Mater.* **20**, 62–67 (2021).
54. Shen, B. et al. Atomic spatial and temporal imaging of local structures and light elements inside zeolite frameworks. *Adv. Mater.* **32**, 1906103 (2020).
55. Benedek, N. A. & Fennie, C. J. Hybrid improper ferroelectricity: a mechanism for controllable polarization-magnetization coupling. *Phys. Rev. Lett.* **106**, 107204 (2011).
56. Choudhury, S., Li, Y., Krilliii, C. & Chen, L. Phase-field simulation of polarization switching and domain evolution in ferroelectric polycrystals. *Acta Mater.* **53**, 5313–5321 (2005).
57. He, L. et al. Large electrostrain with nearly-vanished hysteresis in eco-friendly perovskites by building coexistent glasses near quadruple point. *Nano Energy* **90**, 106519 (2021).

Acknowledgements

This work was supported by the National Natural Science Foundation of China (Grant No. 12204503, No. U2002217), Shanghai Pujiang Program (No. 22PJD085), Key Research Program of the Chinese Academy of Sciences (Grant No. ZDRW-CN-2021-3-1-18), Natural Science Foundation of Shanghai (23ZR1472400), the joint PhD training program of University of Chinese Academy of Sciences and Student Training Program for Innovation and entrepreneurship of Hangzhou Institute for Advanced Study, UCAS (CXCY20230305).

Author contributions

Z.L., and G.S.W. conceived and designed the study. T.D. performed the investigation and curated the data. J.Y.X., L.Q.H., H.N.P., and T.L. contributed to data collection and validation. T.D. led the data analysis. J.Y.X., L.Q.H., D.W., Z.L., B.D., W.B.H., and C.M.-B. contributed to the analysis. Z.C.H., Y.H.C., and Z.S.L. fabricated the MLCCs. T.D. and Z.L. wrote the original draft. Z.L., C.M.-B., G.S.W., B.D., and J.H.C. reviewed and edited the manuscript. G.S.W., D.W., Y.L., and J.H.C. supervised the project. All authors participated in the data analysis and discussions.

Competing interests

The authors declare no competing interests.

Additional information

Supplementary information The online version contains supplementary material available at https://doi.org/10.1038/s41467-026-69279-2.

Correspondence and requests for materials should be addressed to Zhen Liu, Dong Wang or Genshui Wang.

Peer review information *Nature Communications* thanks Mohan K. Bhattarai, and Alexander Martin for their contribution to the peer review of this work. A peer review file is available.